J. Fluid Mech. (1998), *vol.* 360, *pp.* 21–39. Printed in the United Kingdom

Thermocapillary and oscillatory-shear instabilities in a layer of liquid with a deformable surface

By A. C. OR AND R. E. KELLY

Department of Mechanical, Aerospace and Nuclear Engineering,
University of California, Los Angeles, CA 90095-1597, USA

(Received 28 February 1997 and in revised form 27 October 1997)

The thermocapillary and shear-induced instabilities of a thin heated layer of liquid bounded from the top by a deformable free surface and at the bottom by a horizontally oscillating plate are studied for both Earth-bound and microgravity conditions. Finite-wavelength thermocapillary convection can be stabilized very significantly by the oscillatory shear, whereas shear-induced instabilities are greatly stabilized if the Marangoni number is negative. For long-wavelength thermocapillary convection, oscillatory shear can stabilize or destabilize the basic state, depending primarily on the imposed forcing frequency. With microgravity, significant stabilization of the dominant long-wavelength convection can be achieved by carefully selecting the imposed frequency.

1. Introduction

A heated layer of liquid possessing a deformable surface can give rise to both long- and finite-wavelength thermocapillary instabilities. Results concerning the finite-wavelength thermocapillary instability date back to the famous experiment on convection by Bénard (1901), although his results were originally thought to be associated with buoyancy-induced convection. Detailed theoretical analysis of this instability was given by Pearson (1958), and recent experimental results have been reported by Schatz *et al.* (1995). The long-wavelength instability tends to be the dominant instability only in very thin films on Earth; in Space, however, it tends to be always dominant. It was first reported by Scriven & Sternling (1964), and Smith (1966) extended the long-wavelength analysis to include the stabilizing effect of gravity. Recently, an experimental investigation of the long-wavelength instability for a thin layer of liquid was reported by VanHook *et al.* (1995); see also VanHook *et al.* (1997). The experimental results not only confirm the existence of the long-wavelength instability but also illustrate its pronounced connection with surface deformation, which can eventually lead to the formation of dry spots. Needless to say, the rupture of the fluid film would be catastrophic in regard to either thermocapillary heat transfer or materials processing involving such films in Space.

It is therefore of interest to see if these instabilities can be controlled. One method of control involves imposing oscillatory non-planar shear on the liquid layer as shown diagramatically in figure 1. It was discussed by Or & Kelly (1995) for thermocapillary (Marangoni) convection when small-amplitude oscillations occur. They found that oscillatory shear tends to stabilize the finite-wavelength (or Pearson) mode of instability

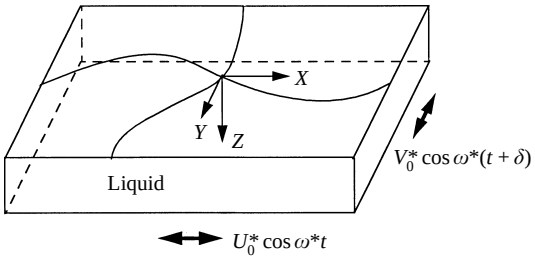

FIGURE 1. Geometrical configuration.

but to destabilize the long-wavelength, deformational (or Scriven–Sternling–Smith) mode of instability. Stabilization of the Pearson mode seems to be akin to the stabilization of Rayleigh–Bénard convection, which Kelly & Hu (1994) have predicted to be quite pronounced on a linear basis for large-Prandtl-number fluids at moderate values of the Reynolds number (< 200). Schatz *et al.* (1995) give experimental results confirming the weakly subcritical nature of the finite-wavelength instability in thermocapillary convection. However, we argue that the results of Hall & Kelly (1995) for the analogous case of Rayleigh–Bénard convection in a fluid with temperature-dependent viscosity, which predict that oscillatory shear converts the subcritical bifurcation into a supercritical one, might hold also for the onset of the present finite-wavelength instability. The shear destroys the horizontal isotropy required for hexagonal convection. The strongly subcritical instability associated with the long-wavelength instability as described by VanHook *et al.* (1997) is more problematical. For that instability we can only discuss the effect of oscillations upon the location of the bifurcation point.

While the results demonstrate that the Pearson mode can, in principle, be strongly stabilized, they also indicate that the deformational mode can be strongly stabilized or destabilized, depending on the frequency of the oscillation. The destabilization is related to the effects of unsteady shear upon the free surface, as discussed for the isothermal situation by Yih (1968) and Or (1997). The regions of instability for the isothermal case as a function of Reynolds number and a non-dimensional parameter β involving the imposed frequency are shown in figure 2 and will be referred to later. The open-ended loops correspond to the large wavelength instability of Yih (1968), while the neutral stability curves branching off the loops have been discussed by Or (1997). These slanted curves are associated with finite-wavelength instabilities except at the branch point itself. Both instabilities can, of course, also occur when the layer is heated and are important in governing the overall stability of the heated layer. Although the Bond and crispation numbers are important in deciding whether the dominant thermocapillary instability consists of finite- or long-wavelength disturbances, the effect of the oscillations upon changing the critical value of the Marangoni number seems to be mainly controlled by the Reynolds number and non-dimensional frequency.

It should be emphasized that, when we refer to 'shear instability', we are referring to the interfacial instability described by Yih (1968) and not to an instability of the basic unsteady shear flow. The reader is referred to the paper by Blondeaux & Vittori (1994) for a survey of results concerning the instability of the Stokes layer. It seems to be clear that nonlinear effects must be considered in order to describe this instability and so it is out of the realm of validity of the present linear analysis. Some additional remarks are made in this regard at the end of the paper. We organize the paper as follows. In § 2, we present the mathematical formulation of the problem. In § 3,

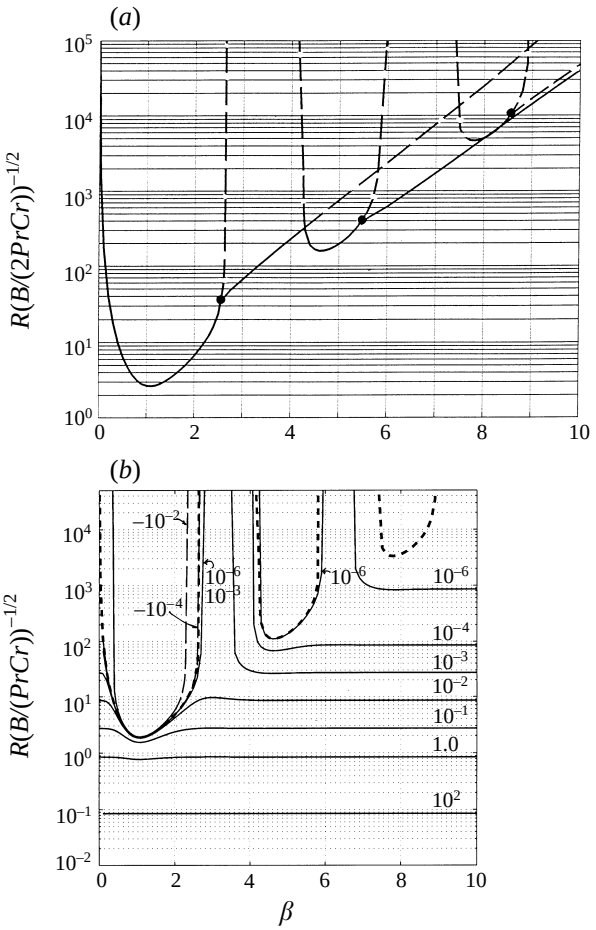

FIGURE 2. (*a*) Neutral curves of the Yih instability plotted in the $(\beta, (L_\beta/2)^{-1/2})$-plane. The neutral curves of the finite-wavelength instability (straight lines) were computed at $PrCr = 0.05$ and $B/2PrCr = 1.0$ (figure reproduced from Or 1997, figure 3*a*). (*b*) Family of neutral curves of the long-wavelength instability with heating effects included. Labels show values of M^*; the isothermal loops are shown as thick dashed lines.

the analysis and results for long-wavelength disturbances are given. We feel that a better understanding of this complicated problem can be obtained by discussing these results before those for arbitrary wavelength disturbances, which is done in § 4. Some concluding remarks are given in § 5.

2. Mathematical formulation

2.1. *Governing equations*

We consider a layer of Boussinesq liquid of infinite horizontal extent and of mean thickness h, bounded below by a rigid horizontal plate and above by a deformable free surface. Either the layer is assumed to be very thin or the effective gravitational acceleration is assumed to be very small so that the buoyancy force can be taken to be negligible. This allows us to focus upon the thermocapillary and interfacial shear instabilities. The plate is isothermal with temperature T_1^*. At the upper surface ($z = 0$),

a mixed thermal boundary condition is applied involving a Biot number so that a temperature difference ΔT^* is maintained across the layer in the undisturbed state. We scale length, time, velocity, pressure and temperature according to h, ω^{*-1}, ν/h, $\rho\nu^2/h^2$ and ΔT^*, where ω^* is the frequency of the external forcing, ν is the kinematic viscosity, and ρ is the reference density of the fluid. The governing non-dimensional Boussinesq equations are then as follows:

$$2\beta^2\partial_t \boldsymbol{v} + \boldsymbol{v}\cdot\nabla\boldsymbol{v} = -\nabla P + \nabla^2\boldsymbol{v}, \tag{1}$$

$$\nabla\cdot\boldsymbol{v} = 0, \tag{2}$$

and

$$2\beta^2\partial_t T + \boldsymbol{v}\cdot\nabla T = Pr^{-1}\nabla^2 T, \tag{3}$$

In the above non-dimensional equations, β is a frequency parameter governing the thickness of the Stokes layer and is defined by $\beta = (\omega^* h^2/2\nu)^{1/2}$, while Pr is the Prandtl number ν/κ. The basic horizontal flow $\boldsymbol{v} = \boldsymbol{U}(z,t)$ satisfies the no-slip boundary condition at the lower surface $z = 1$ (see figure 1) and so

$$U(1,t) = Re\cos t, \tag{4a}$$

$$V(1,t) = \lambda Re\cos(t+\delta), \tag{4b}$$

where the Reynolds number $Re = U_0^* h/\nu$, the velocity ratio $\lambda = V_0^*/U_0^*$, and U_0^* and V_0^* are the amplitudes of the oscillatory motion of the wall in the x- and y-directions, respectively. We also choose our x- and y-directions so that the oscillation in the x-direction has a larger magnitude, i.e. $\lambda < 1$. A time phase of δ is introduced to give a non-planar shear effect. The free surface does not deform due to the basic flow, and so a stress-free condition is imposed on the basic flow at $z = 0$, as follows:

$$\partial_z U(0,t) = \partial_z V(0,t) = 0. \tag{4c}$$

The governing equation for the basic flow $\boldsymbol{U}(z,t)$ is

$$2\beta^2\partial_t \boldsymbol{U} = \partial_{zz}\boldsymbol{U}, \tag{5}$$

where U and V are the two components of $\boldsymbol{U}$. The solution of (5) that satisfies the boundary conditions (4*a–c*) is given by

$$U(z,t) = Re\{\phi_c(z)\cos t + \phi_s(z)\sin t\}, \tag{6a}$$

$$V(z,t) = \lambda Re\{\phi_c(z)\cos(t+\delta) + \phi_s(z)\sin(t+\delta)\}. \tag{6b}$$

The two functions $\phi_c(z)$ and $\phi_s(z)$ are given by

$$\phi_c(z) = \frac{1}{2}\left\{\frac{\cosh(1+\mathrm{i})\beta z}{\cosh(1+\mathrm{i})\beta} + \frac{\cosh(1-\mathrm{i})\beta z}{\cosh(1-\mathrm{i})\beta}\right\}, \tag{7a}$$

$$\phi_s(z) = \mathrm{i}\frac{1}{2}\left\{\frac{\cosh(1+\mathrm{i})\beta z}{\cosh(1+\mathrm{i})\beta} - \frac{\cosh(1-\mathrm{i})\beta z}{\cosh(1-\mathrm{i})\beta}\right\}. \tag{7b}$$

The temperature $\overline{T}(z)$ of the basic state relative to the reference temperature is governed by the steady conduction equation and is given by

$$\overline{T}(z) = z - 1. \tag{8}$$

We now introduce perturbations in the flow and thermal fields by superposing a disturbance velocity with components u, v, and w and a disturbance temperature θ on

the basic state. Upon linearization, we obtain the following perturbation equations:

$$2\beta^2\partial_t u + (U\partial_x + V\partial_y)u + w\partial_z U = -\partial_x p + \nabla^2 u, \tag{9}$$

$$2\beta^2\partial_t v + (U\partial_x + V\partial_y)v + w\partial_z V = -\partial_y p + \nabla^2 v, \tag{10}$$

$$2\beta^2\partial_t w + (U\partial_x + V\partial_y)w = -\partial_z p + \nabla^2 w, \tag{11}$$

$$\partial_x u + \partial_y v + \partial_z w = 0, \tag{12}$$

and

$$2\beta^2 Pr\ \partial_t\theta + Pr(U\partial_x + V\partial_y)\theta = -Pr\ w + \nabla^2\theta. \tag{13}$$

These equations are, respectively, the three linearized momentum equations, the continuity equation, and the thermal energy equation. The bottom-plate boundary conditions at $z = 1$ are

$$u = v = w = \theta = 0. \tag{14}$$

In addition to the above perturbations there is also a surface deformation giving rise to a perturbation height $\eta(x, y, t)$ on the free surface. The boundary conditions at the free surface are evaluated at the mean height $z = 0$. They consist of equations for the normal and tangential stresses, the heat transfer condition and the kinematic condition, as follow respectively:

$$((\partial_x\eta)\partial_z U + (\partial_y\eta)\partial_z V) - \frac{B}{2PrCr}\ \eta\partial_z P + \partial_z w - \frac{p}{2} + \frac{1}{2PrCr}(\partial_{xx} + \partial_{yy})\eta = 0, \tag{15}$$

$$\eta\partial_{zz}U + (\partial_z u + \partial_x w) = MPr^{-1}\left((\partial_z\bar{T})\partial_x\eta + \partial_x\theta\right), \tag{16}$$

$$\eta\partial_{zz}V + (\partial_z v + \partial_y w) = MPr^{-1}\left((\partial_z\bar{T})\partial_y\eta + \partial_y\theta\right), \tag{17}$$

$$Bi(\eta\partial_z\bar{T} + \theta) = \partial_z\theta, \tag{18}$$

$$2\beta^2\partial_t\eta + (U\partial_x + V\partial_y)\eta = w. \tag{19}$$

The additional non-dimensional parameters that appear in the perturbation equations are defined as follows: $M = \gamma\Delta T^* h/\rho\nu\kappa$, $B = \rho g h^2/\sigma$, $Bi = qh/K$, $Cr = \rho\nu\kappa/\sigma h$. These parameters are, respectively, the Marangoni number, Bond number, Biot number and crispation number. The physical quantities involved in the parameters are standard, where γ is the rate of change of surface tension force with respect to temperature, σ is the surface tension for the reference state, α is the coefficient of thermal expansion, q is the surface heat flux, and K is the thermal conductivity. The general system consisting of the six dependent variables u, v, w, p, θ and η, can be reduced to one consisting of three dependent variables, namely w, θ and η (see Or & Kelly 1995). Now we let

$$(w, \theta, \eta) = (W(z,t), \Theta(z,t), N(t))\,\mathrm{e}^{\mathrm{i}(k_x x + k_y y)} + \text{c.c.} \tag{20}$$

where c.c. denotes the complex conjugate. Upon substitution of (20) into (9)–(19), the governing equations are reduced to

$$\left\{2\beta^2\partial_t + \mathrm{i}(k_x U + k_y V - (\partial_{zz} - k^2)\right\}(\partial_{zz} - k^2)W - \mathrm{i}(k_x\partial_{zz}U + k_y\partial_{zz}V)\ W = 0, \tag{21}$$

and

$$Pr\left\{2\beta^2\partial_t + \mathrm{i}(k_x U + k_y V)\right\}\Theta - (\partial_{zz} - k^2)\Theta = -Pr\ W, \tag{22}$$

to be solved subject to the wall boundary conditions (at $z = 1$)

$$W = \partial_z W = \Theta = 0, \tag{23}$$

the free-surface normal stress condition (at $z = 0$)

$$(2\beta^2\partial_{tz} - \partial_{zzz} + 3k^2\partial_z)W - \frac{k^2}{PrCr}(B + k^2)N = -\mathrm{i}(k_x(U\partial_z W + 2k^2 N\partial_z U) - k_y(V\partial_z W + 2k^2 N\partial_z V)), \quad (24)$$

the free-surface shear stress condition

$$\partial_{zz}W + k^2 W - Pr^{-1}Mk^2(N + \Theta) = \mathrm{i}(k_x\partial_{zz}U + k_y\partial_{zz}V)N, \quad (25)$$

and the free-surface thermal and kinematic conditions

$$\partial_z\Theta - B_i(N + \Theta) = 0, \quad (26)$$

$$2\beta^2\partial_t N - W = -\mathrm{i}(k_x U + k_y V)N, \quad (27)$$

where $k^2 = k_x^2 + k_y^2$.

2.2. *Discussion on pattern orientation*

In the governing equations, Re appears as a multiplicative factor in the advective term $\mathrm{i}(k_x U(z,t) + k_y V(z,t))$, which upon substitution from (6*a*, *b*), has the following form:

$$\mathrm{i}Re\{k_x(\phi_c(z)\cos t + \phi_s(z)\sin t) + \lambda k_y(\phi_c(z)\cos(t + \delta) + \phi_s(z)\sin(t + \delta))\}. \quad (28)$$

The bidirectional nature of the above term is apparent. However, there is a way to rewrite the above expression in unidirectional form by introducing an effective Reynolds number, R. With some algebraic manipulation, (28) can be rewritten as

$$\mathrm{i}kR\{\phi_c(z)\cos\hat{t} + \phi_s(z)\sin\hat{t}\}, \quad (29)$$

where the effective Reynolds number, R, is called the non-planar Reynolds number and is given by

$$R(\phi, \lambda, \delta) = Re((\cos\phi + \lambda\sin\phi\cos\delta)^2 + (\lambda\sin\phi\sin\delta)^2)^{1/2}, \quad (30)$$

with

$$k_x = k\cos\phi, \quad k_y = k\sin\phi. \quad (31)$$

The time $\hat{t}$ used in (29) has a time shift involving a phase φ, given by

$$\hat{t} = t + \varphi, \quad \varphi = \sin^{-1}(Re\lambda\sin\phi\sin\delta/R). \quad (32)$$

The ratio R/Re depends on the wave vector direction, ϕ, which is measured counter-clockwise from the x-axis, the amplitude ratio λ, and the phase-lag angle δ. Except for ϕ, these parameters as well as Re are externally imposed. In order to give a maximum non-planar effect, we let $\delta = \pi/2$ (see discussion by Kelly & Hu 1993). The criticality of the onset of convection occurs at the minimum of M, which is a function of k and the non-planar Reynolds number, R, both of which are internal parameters. For $\delta = \pi/2$, we have $R = Re(\cos^2\phi + \lambda^2\sin^2\phi)^{1/2}$. The non-planar Reynolds number has to assume a maximum value when the non-planar shear exerts a destabilizing effect on convection and a minimum value when the shear exerts a stabilizing effect instead. The maximum value of $R = Re$ for $\lambda < 1$ corresponds to $\phi = 0$, i.e. transverse rolls. On the other hand, the minimum value of $R = \lambda Re$ corresponds to $\phi = \pi/2$, i.e. longitudinal rolls. With this result, it is sufficient for us to consider only two types of pattern orientation: (*a*) the purely x-periodic (transverse) mode with $R = Re$, and (*b*) the purely y-periodic (longitudinal) mode with $R = \lambda Re$ (note: $0 < \lambda < 1$).

3. Long-wavelength expansion

This approach is used to obtain results that can be compared directly to the loops in figure 2(*a*) that describe the long-wavelength instability of the isothermal system. As discussed in Or (1997), the results are used eventually also to locate the branch points at which the finite-wavelength stability curves originate. As we shall show, the various non-dimensional parameters combine to form a smaller group, and so the parametric trends can be discussed more easily for long-wavelength than for arbitrary-wavelength disturbances. However, it should be emphasized that the overall stability of the basic state can only be determined by considering finite-wavelength as well as long-wavelength disturbances, and this will be done in § 4. For small k, we express W, Θ and N in the following form:

$$W(z,t) = k(RW_1(z,t) + kR^2\overline{W}_2(z) + \ldots), \tag{33a}$$

$$\Theta(z,t) = (\Theta_0(z) + kR\Theta_1(z,t) + k^2R^2\overline{\Theta}_2(z) + \ldots), \tag{33b}$$

and

$$N(t) = (N_0 + kRN_1(t) + k^2R^2\overline{N}_2 + \ldots). \tag{33c}$$

The overlines on variables denote time-mean quantities, which are the only second-order quantities we need to consider in order to obtain the lowest-order solvability condition. The scaling factor R is introduced to make R appear in the second-order balance. At $O(k^1)$, $W_1(z,t)$ and $\Theta_1(z,t)$ can be expressed as

$$W_1(z,t) = \mathrm{i}(\hat{W}_1(z)\cos t + \check{W}_1(z)\sin t), \tag{34a}$$

$$\Theta_1(z,t) = \mathrm{i}(\hat{\Theta}_1(z)\cos t + \check{\Theta}_1(z)\sin t), \tag{34b}$$

$$N_1(t) = \mathrm{i}(\hat{N}_1\cos t + \check{N}_1\sin t). \tag{34c}$$

The following complex notation will be used shortly:

$$\Phi = \phi_c + \mathrm{i}\phi_s, \tilde{W}_1 = \hat{W}_1 + \mathrm{i}\check{W}_1, \tilde{\Theta}_1 = \hat{\Theta}_1 + \mathrm{i}\check{\Theta}_1, \tilde{N}_1 = \hat{N}_1 + \mathrm{i}\check{N}_1.$$

(i) $O(k^0)$

At this order, only the thermal and surface displacement effects appear. The governing equations and boundary conditions evaluated at $z = 0$ and at $z = 1$ are

$$\mathrm{D}^2\Theta_0 = 0, \quad \mathrm{D}\Theta_0(0) - Bi\ \Theta_0(0) = Bi\ N_0, \quad \Theta_0(1) = 0, \tag{35}$$

where $\mathrm{D}f = \mathrm{d}f/\mathrm{d}z$. The solution is obtained as

$$\Theta_0(z) = \frac{Bi\ N_0}{1 + Bi}(z - 1). \tag{36}$$

The constant N_0 will remain arbitrary.

(ii) $O(k^1)$

The governing equations for velocity and temperature are more conveniently treated in a complex form; these are, respectively,

$$\mathrm{i}2\beta^2\mathrm{D}^2\tilde{W}_1 + \mathrm{D}^4\tilde{W}_1 = 0, \tag{37a}$$

and

$$\mathrm{i}2\beta^2 Pr\tilde{\Theta}_1 + \mathrm{D}^2\tilde{\Theta}_1 - Pr\tilde{W}_1 = -Pr\Phi\Theta_0. \tag{37b}$$

These equations are solved subject to the homogeneous wall boundary conditions

$$\tilde{W}_1(1) = \mathrm{D}\tilde{W}_1(1) = \tilde{\Theta}_1(1) = 0 \tag{37c}$$

and to the free-surface conditions at $z = 0$ involving the normal and tangential stresses, as well as the kinematic and the heat transfer conditions:

$$\mathrm{D}^3\tilde{W}_1(0) + \mathrm{i}2\beta^2\mathrm{D}\tilde{W}_1(0) = 0, \quad \mathrm{D}^2\tilde{W}_1(0) - \mathrm{D}^2\Phi(0) = 0, \tag{37d}$$

$$\tilde{W}_1(0) + \mathrm{i}2\beta^2\tilde{N}_1 = \Phi(0), \quad \mathrm{D}\tilde{\Theta}_1(0) = Bi\ (\tilde{N}_1 + \tilde{\Theta}_1(0)). \tag{37e}$$

The solution $\tilde{W}_1(z)$ is identical to the isothermal solution $\tilde{W}_0(z)$ at $O(k)$ given in Or (1997, 3.3(*a–c*)). At this order the disturbance flow field generates a thermal field which is not coupled with it. There are altogether seven boundary conditions. Both the kinematic and heat transfer boundary conditions involve N_1, which is an unknown. We can first eliminate $\tilde{N}_1$ from the seven conditions to give six boundary conditions, so that a matrix inversion of the system gives $\tilde{W}_1(z)$ and $\tilde{\Theta}_1(z)$. Then we solve for $\tilde{N}_1$ from one of the conditions. We now proceed to the $O(k^2)$ problem.

(iii) *Second-order mean field balance*
At this order, the mean field equations are

$$\mathrm{D}^4\overline{W}_2 = -\tfrac{1}{2}(\phi_c\mathrm{D}^2\hat{W}_1 + \phi_s\mathrm{D}^2\check{W}_1) + \tfrac{1}{2}(\mathrm{D}^2\phi_c\hat{W}_1 + \mathrm{D}^2\phi_s\check{W}_1), \tag{38a}$$

$$\mathrm{D}^2\overline{\Theta}_2 - Pr\overline{W}_2 = \tfrac{1}{2}Pr(\phi_c\hat{\Theta}_1 + \phi_s\check{\Theta}_1). \tag{38b}$$

The boundary conditions at $z = 1$ are

$$\overline{W}_2(1) = \mathrm{D}\overline{W}_2(1) = \overline{\Theta}_2(1) = 0. \tag{38c}$$

The free-surface conditions at $z = 0$ are

$$\mathrm{D}^3\overline{W}_2(0) = -L_\beta N_0 - \tfrac{1}{2}(\phi_c(0)\mathrm{D}\hat{W}_1(0) + \phi_s(0)\mathrm{D}\check{W}_1(0)), \tag{38d}$$

$$\mathrm{D}^2\overline{W}_2(0) = M^*(N_0 + \Theta_0(0)) - \tfrac{1}{2}(\mathrm{D}^2\phi_c(0)\hat{N}_1 + \mathrm{D}^2\phi_s(0)\check{N}_1), \tag{38e}$$

$$\overline{W}_2(0) = -\tfrac{1}{2}(\phi_c(0)\hat{N}_1 + \phi_s(0)\check{N}_1). \tag{38f}$$

and

$$\mathrm{D}\overline{\Theta}_2(0) - Bi\ \overline{\Theta}_2(0) = Bi\ \overline{N}_2. \tag{38g}$$

The non-dimensional groups defined by

$$L_\beta = \frac{B}{PrCrR^2}, \quad M^* = \frac{M}{PrR^2}, \tag{39}$$

serve to reduce the group of parameters consisting of B, Cr, R and M, to two parameters. Note that L_β for the isothermal situation is identical to the parameter $L(\beta)$ defined in Or (1997). Together with Bi, which appears at lowest order, and β and Pr, which appear at first order, we have altogether five non-dimensional groups as $k \to 0$ for the boundary-value problem posed by (38*a–g*). This problem can be solved by standard numerical methods.

According to Takashima (1981), for example, the critical Marangoni number of the

long-wavelength mode of convection with no shear modulation is given by

$$M_c = \frac{2}{3}\frac{B}{Cr}(1 + Bi). \tag{40}$$

On the other hand, according to Yih (1968) and Or (1997), the critical Reynolds number under shear but with an isothermal condition ($M = 0$) is given by

$$R = \left(\frac{B}{L_\beta PrCr}\right)^{1/2}. \tag{41}$$

We use R in the above expression instead of Re to avoid unncessary confusion involving the problem of pattern orientation. In applications, R should be interpreted as Re if the shear decreases M and as λRe if the shear increases M. Both situations assume that $M > 0$.

Figure 2(b) shows, for $Pr = 7$ and $Bi = 0.1$, the family of neutral curves for the long-wavelength instability as $k_c \to 0$ in the $(\beta, L_\beta^{-1/2})$-plane parameterized by imposing the value of M^*. The region above a curve is unstable and below it stable. The three dashed loops correspond to the isothermal case at $M = 0$ and are the same as the loops shown in figure 2(a), except now on an ordinate scale smaller by a factor of $\sqrt{2}$. The thinner solid curves are labelled by a number on the right-hand side of the figure indicating the value of M^*. For $M^* > 0$, the loop structure disappears as M^* increases. Gradually, the curvature of the neutral curves disappears and the neutral boundaries tend to horizontal straight lines. As M^* increases, so does the critical value of L_β. As L_β and M^* both become large, $M^* \to 2(1 + Bi)L_\beta/3$, corresponding to the limit of no shear (see (40)). The discussion at the end of § 4 has more remarks in this limit. When $M^* < 0$, the loop curves reside in the interior of the regions bounded by the dashed loops. For $M^* = -10^{-2}$, corresponding to a stabilizing thermal gradient, only the first loop remains as shown. The second and third loops have disappeared, indicating no instability at higher β. In fact, for M^* as small as -10^{-4}, the second and third loops have already disappeared, whereas at this small M^* the first loop almost coincides with the dashed line. The above results show that for $M > 0$ the Marangoni effect and the interfacial shear effect reinforce each other to produce a stronger instability. But for negative M the thermal effect strongly stabilizes Yih's instability.

The shapes of the neutral curves of figure 2(b) shed some light on the frequency dependence of the long-wavelength instability. For $R \neq 0$ we can eliminate the dependence on R from the two parameters, L_β and M^* to obtain $M = (BCr^{-1}M^*)L_\beta^{-1}$. By staying on a neutral curve, say, $M^* = 10^{-2}$, M only depends on the ordinate L_β^{-1}. The curve is almost flat for $\beta > 3$. At a slightly smaller β, there is a small elevation (which becomes more pronounced at even smaller M^*). Further decrease in β will drive the curve into a dip with minimum around $\beta = 1.1$. Relative to its value at $\beta = 0$, the ordinate of the curve indicates whether the shear is stabilizing or destabilizing with regard to the long-wavelength convection. Thus, examining the neutral curve with $M^* = 10^{-2}$, for example, the shear is destabilizing around $\beta = 1.1$ but mildly stabilizing near $\beta = 3.0$. At very large β, the vertical value of a point on the curve equals that at $\beta = 0$, suggesting that the shear effect vanishes.

The purpose of figure 2(b) is to provide the global view of the family of the neutral curves. For ease in interpretation of results, it is worthwhile to compute specific neutral curves as functions of frequency to gain more detailed information. We now present some results from the long-wavelength analysis which might eventually be

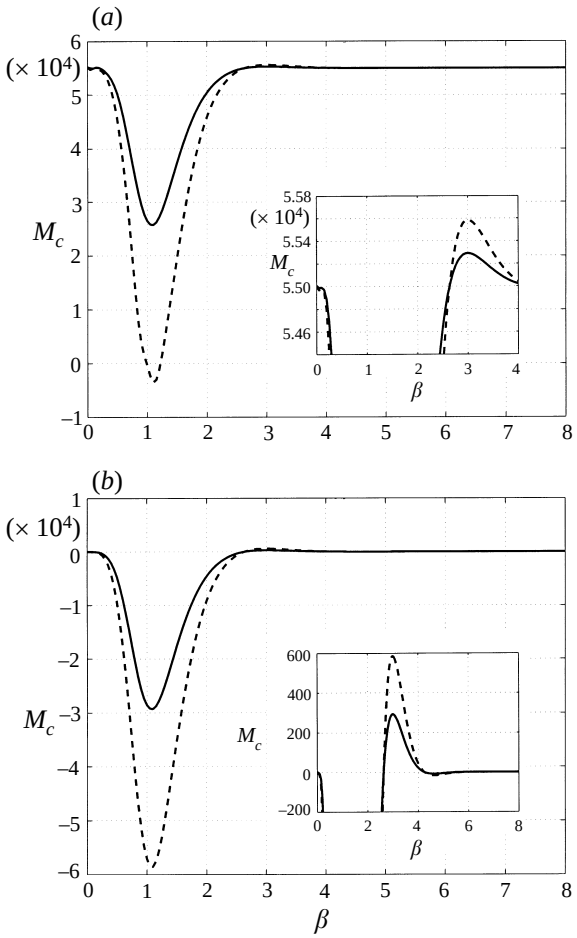

FIGURE 3. (*a*) Long-wavelength critical curves at the Earth-bound condition for longitudinal (solid line) and transverse (dashed line) mode, showing the dependence of shear-induced stabilization and destabilization on modulation frequency. Insert shows a magnified view near the stabilization portion of the critical curves. (*b*) As (*a*) except at the microgravity condition.

used to compare with results of laboratory experiments. The parameters used are based on water at room temperature. We let $\nu = 0.01$ cm^2 s^{-1}, $\kappa = 0.0014$ cm^2 s^{-1}, $\sigma = 73$ dyne cm^{-1}, $\rho = 1$ g cm^{-3} and $h = 0.1$ cm. Say that the experiment is done on Earth. These physical parameter values translate into the following non-dimensional group values: $Pr = 7$, $Cr = 1.9 \times 10^{-6}$ and $B = 0.15$. For such a layer, a temperature difference across the layer of 0.1°C will give $M \approx 115$ but a Rayleigh number of ≈ 7. This latter value is so small that the neglect of the buoyancy effect is indeed justified. In the numerical study we used $Cr = 2.0 \times 10^{-6}$ and $B = 0.15$ for the Earth-bound case. However, $B = 0.15 \times 10^{-5}$ is used for the microgravity case. The Biot number was set at 0.1. The range of β used corresponds to $\omega^* < 32$ Hz.

We begin by presenting the stability limit of the deformation instability in a plane of M versus β, based on the long-wavelength solvability condition. Figure 3(*a*) presents the Earth-bound case when, without shear, the Pearson mode tends to be more unstable; we will compare results for the various modes later. Both stability curves correspond to $Re = 200$ but their effective Reynolds numbers are different. The solid

line shows the neutral curve for the longitudinal mode ($\theta = \pi/2$) at $R = \sqrt{0.5}Re$ and $\delta = \pi/2$. The dashed line shows the neutral curve for the transverse mode ($\theta = 0$) at $R = Re$. Since the depth of the dips of the curves in the figures is significantly larger than the height of the peaks, we magnify in the inserts to figures 3(a, b) the peak portions on an enlarged scale for clarity. As $\beta \to 0$, M assumes the value at the purely thermocapillary limit, regardless of the value of Re because the shear vanishes as $\beta \to 0$. As β increases, the neutral curve starts to dip indicating that the oscillatory shear destabilizes thermocapillary convection for low values of β. The minimum for the dashed curve occurs at $M = -0.3 \times 10^4$ and that for the solid one at $M = 2.6 \times 10^4$, near $\beta = 1.1$. The dip occurs within the band of frequencies characteristic of the first unstable loop in figure 2(a, b), which is reasonable. An interesting result is that, as β further increases, the pair of stability curves shoots up rapidly and gives rise to a narrower band of frequencies within which shear acts instead to stabilize the long-wavelength convection. The maxima of M for stabilization of the longitudinal and transverse disturbances are approximately 5.53×10^4 and 5.56×10^4, respectively, at approximately $\beta = 3.0$. Only very moderate stabilization for the Earth-bound case is possible from the shear effect (less than 0.55% increase in M from the unmodulated value). These results appear consistent with those obtained earlier using the small-Reynolds-number expansion (see figure 3 of Or & Kelly 1995). The depth of the dip and the height of the peak of the neutral curve from its value at $\beta = 0$ appear to be scaled according to Re^2.

Next, we consider the microgravity condition, again for $Re = 200$. For this case, M_c has the small value of 0.5 at $\beta = 0$, suggesting that a steady layer can be extremely unstable to long-wavelength convection even with a very small temperature gradient. The deformational mode is the critical mode when $Re = 0$ for this case. Figure 3(b) again shows a dip centred near $\beta = 1.1$, at values of approximately $M = -2.9 \times 10^4$ for the longitudinal (solid line) mode and $M = -5.8 \times 10^4$ for the transverse (dashed line) mode. Compared with figure 3(a), the dip appears deepened by reducing the Bond number. However, the maxima in M also appear more pronounced. The maxima of M again occur near $\beta = 3.0$, with peaks at about 300 for the longitudinal mode and 600 for the transverse mode, indicating that very substantial stabilization is, in principle, possible.

The minimum and maximum of M again appear to occur near $\beta = 1.1$ and $\beta = 3.0$, respectively, independently of Re. For the isothermal case, these frequencies correspond to the minimum of Re for the first unstable band and to a frequency slightly to the left of the midpoint of the region between the first two unstable bands. With $M \neq 0$, strong stabilization is also evident in figure 2(b) near $\beta = 3$. The degree of stabilization at $\beta = 3.0$, defined by $M(Re)/M(0)$, is shown in figure 4 with $Re = 200$ as a function of B and Pr. Figure 4(a) shows that as B approaches 1, this stabilization factor approaches 1 also. As B tends to zero, $M(0)$ decreases towards zero, consistent with the result of Scriven & Sternling (1964). The increase in the stabilization ratio is most pronounced for $B \ll 1$. Since Cr only appears in the term $B/PrCr$ in the long-wavelength limit, the dependence of the stabilization factor on Cr can be inferred from that of B, shown in figure 4(a). Regarding the Prandtl number, the curve in figure 4(b) shows that the stabilization factor increases linearly in Pr for the microgravity case for the range shown; the results of Hu & Kelly (1997) for Rayleigh–Bénard convection suggest that an asymptotic value exists for very large values of Pr. Finally, if we vary Bi while keeping Pr at 7.0, other results not presented here show that the stabilization factor assumes a constant value at 533.7 over a wide range of Bi from 0.1 to 10^3, indicating that the mechanism

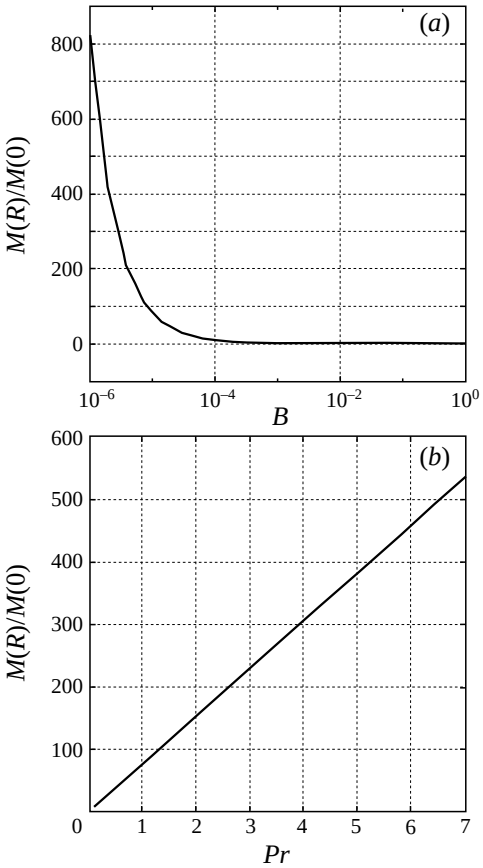

FIGURE 4. The dependence of the maximal stabilization factor $M(Re)/M(0)$ for $Re = 200$ on (*a*) B and (*b*) Pr.

of stabilization is independent of the thermal boundary condition, although $M(0)$ depends on Bi.

4. The fully numerical results

We first describe briefly the method and then proceed to the results. The system of equations (21)–(27) can be solved in two steps. First, we expand the dependent variables in series form through a set of known spatial functions. Here we use the Chebyshev polynomials. We then truncate the number of spatial functions for W to $N_T + 4$ and for Θ to $N_T + 2$, since there are four boundary conditions for the fourth-order equation governing W and two boundary conditions for the second-order equation governing Θ. The boundary conditions are imposed by using the tau method. This numerical procedure yields a finite matrix equation of the following form:

$$2\beta^2 \boldsymbol{B}\dot{\boldsymbol{x}} = \boldsymbol{A}\boldsymbol{x} + \mathrm{i}\boldsymbol{F}(t)\boldsymbol{x}, \tag{42}$$

where all the matrices are real; $\boldsymbol{B}$ and $\boldsymbol{A}$ are time-independent and $\boldsymbol{F}(t)$ is 2π-periodic. The state vector consists of an arrangement of the Chebyshev coefficients for W and Θ and the deformation N.

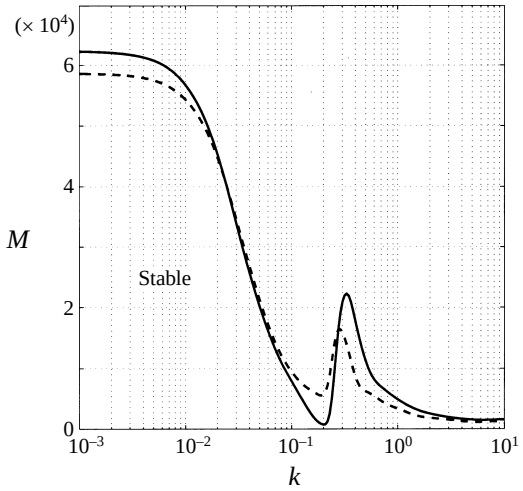

FIGURE 5. A pair of neutral curves showing multiple extrema in wavenumber dependence. The non-planar shear has $Re = 1000$, $\beta = 3.5$, and is for the earth-bound condition. Solid (dashed) line corresponds to the transverse (longitudinal) mode.

The matrix equation has an explicit time dependence. In order to solve it, the second step is to apply Floquet theory by expanding x in standard Fourier series. Since it has been shown that there are no subharmonic solutions when the modulation term is purely imaginary (see Or 1997), we consider only synchronous solutions in the form of

$$\boldsymbol{x}(t) = \sum_{n=-N_p}^{N_p} \boldsymbol{X}_n \, \mathrm{e}^{\mathrm{i}nt+\sigma t}, \tag{43}$$

where σ is the Floquet exponent. The vector functions $\boldsymbol{X}_n$ are constants. The Fourier series is truncated to $2N_p + 1$ terms in temporal modes. For our problem, numerical convergence in the iterated parameter requires more temporal modes than spatial modes. We typically use $N_T = 14$ and $N_p = 24$ to 28 to obtain numerical convergence. The two-step numerical procedure appears standard and has been described in more detail in the appendices of Or (1997).

Upon substitution of expression (43) into (42) we can place all the vector Fourier coefficients into a single matrix eigenproblem. This system is tridiagonal but very large typically. Rather than computing the augmented eigenproblem we use a fast iterative approach which is Newton–Raphson based (see Or 1997). The iterative approach is fast but it depends crucially on a good initial guess for obtaining a solution. Difficulties in convergence in tracing a rapidly varying curve can be overcome by developing iterations on a choice of different parameters; the most common iterate is M, but here k, Re and β are also used as iterates occasionally. When operating in the parameter regime where multiple modes are common, there is no guarantee that the neutral curve obtained through the iterative method corresponds to M_c. Here, extreme care in handling the computations has been taken; in particular, we use small increments for the iterate and use automatic sweeps in the parameter range to minimize the possible omission of new modes.

In order to determine in general the stability regions, it is necessary to compute the neutral curves for a continuous range of k to locate the critical value. As an illustration, in figure 5 we present a pair of neutral curves in k corresponding to

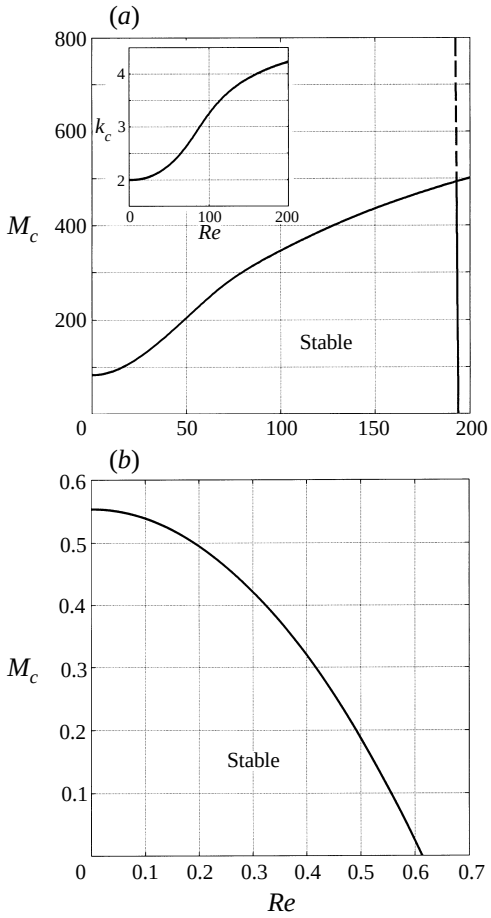

FIGURE 6. Stability region bounded by the neutral curves (the solid portions show critical curves) of several instabilities when arbitrary-wavenumber disturbances are included. The curves are computed at $\beta = 1.1$ for (*a*) Earth-bound and (*b*) microgravity conditions.

the transverse (solid line) and the longitudinal (dashed line) mode for Earth-bound conditions. We consider a case of strong shear, $Re = 1000$, so that multiple minima can be captured within a moderate scale of M in the plot. The frequency corresponds to $\beta = 3.5$. Figure 5 serves as an example for coexisting multiple extrema when the long-wavelength and Pearson modes are well-separated in M. Three stationary points are present, which represent three modes of instabilities. Besides the long-wavelength mode as $k \to 0$ and the Pearson mode at $k \sim O(1)$, there is a minimum of M at an intermediate wavenumber of $O(10^{-1})$, more precisely at $k = 0.2$. This corresponds to the finite-wavelength shear instability reported earlier by Or (1997). The pair of curves intersect at multiple points, indicating that the non-planar shear has different effects on the various instabilities depending on roll orientation. Only by presenting both neutral curves of the longitudinal and transverse modes over the full range of the three instabilities can we conclude that the critical mode for this case is the finite-wavelength shear instability in the transverse mode (solid curve). The critical value is $M_c = 773.2$ and $k_c = 0.2$.

Given the complicated nature of figure 5, determination of the maximal degree of

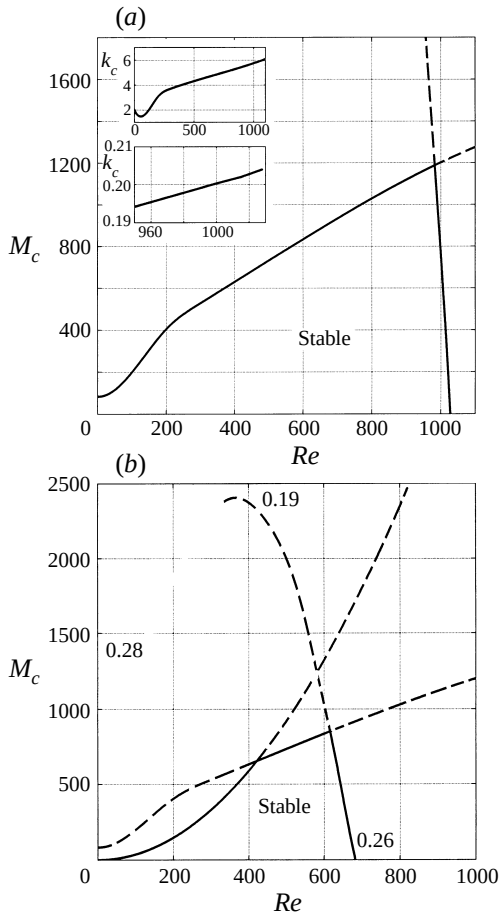

FIGURE 7. Similar to figure 6 except at $\beta = 3.5$. The upper and lower inserts to (a) correspond to k_c for the Pearson and finite-amplitude shear modes.

stabilization or destabilization as a function of β for finite-k convection can be quite a formidable task, since for each β we have to do a sweep on k to determine the critical value of wavenumber. The stabilizing and destabilizing effects on convection, however, can be featured at selected β values, such as $\beta = 1.1$, which corresponds to the most destabilizing frequency for long-wavelength instability, and at $\beta = 3.5$, which is slightly larger than the value for maximum stabilization.

In the next two figures, figures 6(a, b) and 7(a, b), we show the regions where cross-over occurs between the long-wavelength and finite-wavelength neutral curves for the two cases of Earth-bound gravity and microgravity. At $\beta = 1.1$, figure 6(a) corresponds to the Earth-bound case where finite-wavelength disturbances are most unstable, and 6(b) corresponds to the microgravity condition where long-wavelength disturbances dominate. According to the previous analysis by Or (1997), the codimension-two point shown in figure 2 where the finite-k neutral curve branches out from the first loop occurs at $\beta = 0.98$ for this set of parameters. Hence, the long-wavelength and finite-wavelength shear instabilities are almost indistinguishable at $\beta = 1.1$. At Earth-bound gravity, figure 6(a) shows on the right that the long-wavelength neutral curve ramps down steeply so that it represents a barrier for the gently

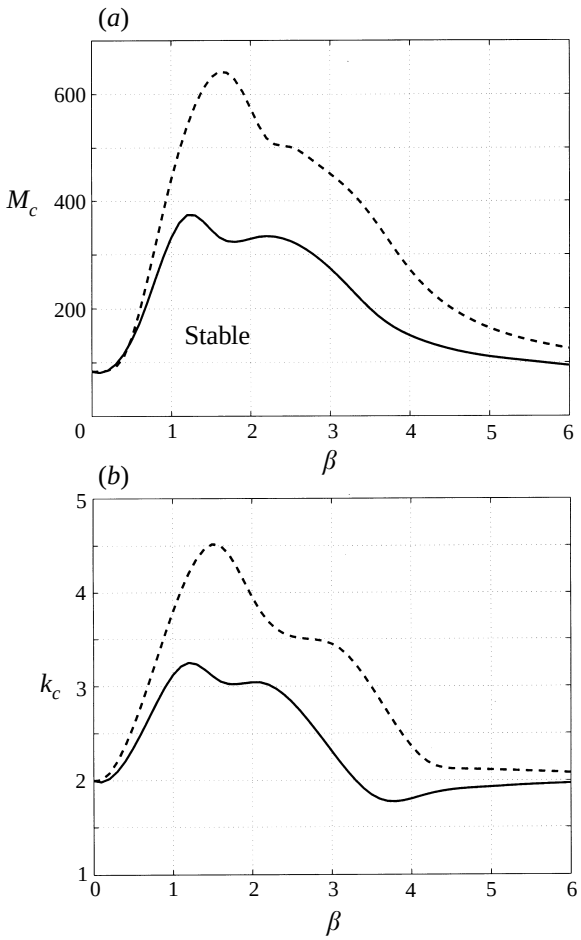

FIGURE 8. (*a*) Critical curves of the Pearson mode corresponding to longitudinal rolls showing the dependenece of the stabilizing effect on β and Re. The solid (dashed) line corresponds to $Re = 100$ ($Re = 193$); (*b*) the corresponding k_c.

increasing neutral curve corresponding to the longitudinal rolls of the Pearson mode of convection, which are stabilized by the shear. The cross-over occurs at about $Re = 192$. Since the cut-off curve is very steep, the value of Re at the cross-over point is approximately equal to that for the isothermal value at $M = 0$ (see figure 2). Beyond $Re = 192$, long-wavelength convection replaces the Pearson mode of convection as the dominant unstable mode. In the inserted panel of figure 6(*a*), we show the change in the critical wavenumber of the Pearson rolls as Re increases. Keeping the other parameters unchanged, we now switch to the microgravity condition by changing B only. The value of B for microgravity is a factor of 10^{-5} smaller than the Earth-bound value. From figure 6(*b*), the stability diagram looks quite different. Because the long-wavelength instability now occurs at a much smaller value of M for $Re = 0$ than that for the Pearson mode, the latter mode of instability need not be considered. It is clear that shear modulation destabilizes the long-wavelength mode, as indicated earlier in regard to figures 2(*b*) and 3(*a*).

Similar to figures 6(*a*) and 6(*b*) but for the higher $\beta = 3.5$, the stability curves for the Earth-bound and microgravity cases are shown in figures 7(*a*) and 7(*b*). For

the Earth-bound case figure 7(*a*) shows two neutral curves crossing in a very similar manner to the ones at $\beta = 1.1$, although at a much larger value of *Re*. Here, at $\beta = 3.5$, Yih's long-wavelength instability is no longer present, and the steep barrier curve is now identified with the finite-wavelength modulated shear instability found by Or (1997). Similar to figure 6(*a*), shear stabilization occurs in the non-planar case for the Pearson mode, as indicated by the gently increasing neutral curve in *Re*. The maximal stabilization here is larger than in figure 6(*a*) because the cut-off *Re* for this case is almost 5 times the previous value. At $\beta = 3.5$, the critical wavenumbers for both stability curves are finite in figure 7(*a*). The inserted panels, however, show that the two k_c differ by an order of magnitude or more. The gently increasing neutral curve corresponds to a longitudinal mode. The neutral curve on the right that acts as a barrier corresponds to the transverse mode. In figure 7(*b*), the neutral curve for long-wavelength convection is the solid curve starting at $M_c = 0.55$ when $Re = 0$ and, along it, M_c increases with *Re*. This curve is the boundary of the stable region until *Re* reaches a value of 425. Between $Re = 425$ and 615, the Pearson mode of convection becomes favoured. Beyond $Re = 615$, the finite-k oscillatory-shear instability studied by Or (1997) acts as the stability barrier. The prediction then is that M_c can be increased from 0.55 for the long-wavelength mode to 846.5 for the Pearson mode (at $k_c = 4.7$) by the use of a non-planar oscillatory shear. The cut-off occurs at $Re = 615$ from the emergence of a finite-k shear instability (transverse rolls) at a critical wavenumber of 0.25 which replaces the Pearson mode (longitudinal rolls) as the preferred mode of convection. We conclude that the modulating frequency is an essential parameter since its value determines whether the long-wavelength convection is stabilized or destabilized by the shear.

Figures 6(*a*) and 7(*a*) indicate that the Pearson mode can be stabilized by the use of unsteady shear at two discrete frequencies, and so it is of interest to show how the amount of stabilization varies as a function of the frequency. Figure 8 presents results for two different values of *Re*, one being near the cut-off value. Figure 8(*a*) indicates that the optimal frequency is somewhat dependent upon the value of *Re* but that significant stabilization occurs over a wide enough range of β that stabilization can be obtained without precise tuning. Figure 8(*b*) shows the critical wavenumber as a function of frequency for the two cases.

5. Summary and conclusion

Thermocapillary convection (without modulation) can occur on a linear basis via either the finite-wavelength Pearson mode or the long-wavelength Scriven–Sternling–Smith mode. Or & Kelly (1995) demonstrated by means of a small-amplitude expansion that an imposed non-planar periodically modulated shear can stabilize the Pearson mode but can also destabilize the long-wavelength mode. The stabilization by unsteady shear is akin to the stabilization of Rayleigh–Bénard convection discussed by Kelly & Hu (1993, 1994). The destabilization was thought by Or & Kelly (1995) to be connected to the long-wavelength interfacial instability found by Yih (1968) for an isothermal layer with a free surface undergoing periodic shear, but nothing definite could be said due to the limitations of the analysis. For this reason, as well as to establish the extent of possible stabilization or destabilization, the analysis for finite-amplitude modulation was carried out, and the results are reported here. This extension was done with the knowledge that Or (1997) has shown that a finite-wavelength mode of instability also occurs for the isothermal problem.

The approach in this paper was to investigate the problem first for long-wavelength disturbances, in which case a smaller group of non-dimensional parameters governs the onset of instability. In comparing the isothermal layer results of figure 2(*a*) to the heated layer results of figure 2(*b*), it is clear that the thermocapillary effect can have a strong influence upon the tongues of instability associated with the interfacial instability discovered by Yih (1968), first causing them to occur only at low frequencies of modulation and ultimately eliminating the banded structure. Conversely, the curves for constant M^* equal to 10^{-1} and 10^{-2} show destabilization near $\beta \approx 1$ which corresponds to the most dangerous frequency in the isothermal case. This effect is shown even more graphically in figures 3(*a*) and 3(*b*) for a fixed value of Reynolds number and two different values of Bond number. Hence, if one wishes to stabilize the basic state, it is important to operate away from the most dangerous frequencies associated with the isothermal situation. Assuming that this is done, figures 4(*a*) and 4(*b*) indicate that long-wavelength disturbances can be greatly stabilized at the low values of Bond number characteristic of the microgravity case and at high values of Prandtl number.

In order to obtain an overall description of the stable regions, finite-wavelength disturbances also had to be considered. The Pearson mode of instability, which is dominant on Earth except for very thin layers, tends to be stabilized over a broad range of frequencies, as shown in figure 8(*a*). The extent of the stable region on Earth is fixed as Re increases by the destabilization and eventual dominance of the Scriven–Sternling–Smith mode for the lower value of frequency or the Or mode at the higher value. For $\beta = 3.5$, the value of M_c is increased by an order of magnitude based on the current analysis. For the microgravity condition, the Scriven–Sternling–Smith mode tends to be dominant and is destabilized by the unsteady shear, as seen in figure 6(*b*), if the frequency is tuned to the most dangerous value for the Yih instability. For a higher value of frequency, however, this mode is stabilized, as shown in figure 7(*b*), so that the Pearson mode becomes more critical. The maximal amount of stabilization is controlled by the Or mode.

Our main conclusion is that stabilization of thermocapillary convection can be achieved both on Earth and in a microgravity environment as long as the frequency of modulation can be controlled. Precise control of the frequency is not required as long as the frequency is not close to the most critical value for the Yih instability. In order to increase heat transfer at small values of Marangoni number, however, the frequency should be as close to the most critical frequency as possible.

In order to place the above results in perspective, some remarks on the possible shear instability of the isothermal Stokes layer are in order. Research results for this problem have been reported in terms of a Reynolds number Re_δ based on the thickness of the Stokes layer and related to the Reynolds number used in this paper by formula $Re_\delta = \beta^{-1} Re_h$. There is by no means universal agreement among experimentalists as to the value of $Re_{\delta,c}$ and a theoretical value does not seem to exist; see the paper by Blondeaux & Vittori (1994). There is more general agreement that the value for transition is $Re_{tr} \approx 500$. If this value is used as an estimate, then the values of Re_h used for the most part in this paper would correspond to the laminar regime for a Stokes layer in an isothermal fluid. Further research on this aspect of the problem is required in order to define fully the stable regions.

This research has been supported by the NASA Microgravity Fluid Physics Program through Grant NAG3-1819.

REFERENCES

Bénard, H. 1901 Les tourbillons cellulaires dans une nappe liquide transportant de la chaleur par convection en régime permanent. *Ann. Chem. Phys.* **23**, 62–144.

Blondeaux, P. & Vittori, G. 1994 Wall imperfections as a triggering mechanism for Stokes-layer transition. *J. Fluid Mech.* **264**, 107–135.

Hall, P. & Kelly, R. E. 1995 Effect of a shear flow on the planform of thermal convection in a fluid of variable viscosity. *Phy. Rev.* **52**, 3687–3696.

Hu, H. C. & Kelly, R. E. 1997 Stabilization of longitudinal vortex instabilities by means of transverse flow oscillations. *Phys. Fluids* **9**, 648–654.

Kelly, R. E. & Hu, H. C. 1993 The onset of Rayleigh–Bénard convection in non-planar oscillatory flows. *J. Fluid Mech.* **249**, 373–390.

Kelly, R. E. & Hu, H. C. 1994 The effect of finite amplitude nonplanar flow oscillations upon the onset of Rayleigh–Bénard convection. *Heat Transfer 1994, Proc. 10th Intl Heat Transfer Conf.* vol. 7, pp. 79–83.

Or, A. C. 1997 Finite wavelength instability in a horizontal liquid layer on an oscillating plane. *J. Fluid Mech.* **335**, 213–232.

Or, A. C. & Kelly, R. E. 1995 Onset of Marangoni convection in a layer of fluid modulated by a weak nonplanar oscillatory shear. *Intl J. Heat Mass Transfer* **38,** 2269–2279.

Pearson, J. R. A. 1958 On convection cells induced by surface tension. *J. Fluid Mech.* **4**, 489–500.

Schatz, M. F., VanHook, S. J., McCormick, W. D., Swift, J. B. & Swinney, H. L. 1995 Onset of surface-tension-driven Bénard convection. *Phys. Rev. Lett.* **75**, 1938–1941.

Scriven, L. E. & Sternling, C. V. 1964 On cellular convection driven surface tension gradients: effects of mean surface tension and surface viscosity. *J. Fluid Mech.* **19**, 321–340.

Smith, K. A. 1966 On convective instability induced by surface tension. *J. Fluid Mech.* **24**, 401–414.

Takashima, M. 1981 Surface tension driven instability in a horizontal liquid layer with a deformable free surface. I. stationary convection. *Phys. Soc. Japan* **50**, 2745–2750.

VanHook, S. J., Schatz, M. F., McCormick, W. D., Swift, J. B. & Swinney, H. L. 1995 Long-wavelength instability in surface-tension-driven Bénard convection. *Phys. Rev. Lett.* **75**, 4397–4400.

VanHook, S. J., Schatz, M. F., Swift, J. B., McCormick, W. D. & Swinney, H. L. 1997 Long-wavelength surface-tension-driven Bénard convection: experiment and theory. *J. Fluid Mech.* **345**, 45–78.

Yih, C. S. 1968 Instability of unsteady flows or configurations Part 1. Instability of a horizontal liquid layer on an oscillating plane. *J. Fluid Mech.* **31**, 737–751.